J Vis (2010) 13:97–105
DOI 10.1007/s12650-009-0019-0

REGULAR PAPER

Kazuya Seo · Osamu Kobayashi · Masahide Murakami · Daisuke Yorita · Hiroki Nagai · Keisuke Asai

Simulation of the trajectory of a punted rugby ball taking into account the asymmetrical pressure distribution caused by the seams

Received: 28 April 2009 / Accepted: 8 December 2009 / Published online: 8 January 2010

Abstract This paper describes the effect of the seams of a rugby ball on the side force and the flight trajectory of the punted kick. Measurement of the aerodynamic force on a non-spinning rugby ball reveals that the side force coefficient depends on the position of the seam as well as the angle of attack. It was found from pressure-sensitive paint measurements that the seam of the ball is the trigger for initiating low pressure when the seam is situated around 60° from the stagnation point. The flight trajectory of the fluctuating ball can be obtained by numerically integrating the six degree-of-freedom non-linear equations of motion. It was shown that a slower spinning ball fluctuates from side to side during flight because of the asymmetrical pressure distribution on the sides of the ball.

Keywords Pressure-sensitive paint · Rugby · Punted kick · Fluctuating flight trajectory · Wind tunnel test

List of symbols

C_Y	Side force coefficient
D	Drag (N)
g	Gravitational acceleration (m s^{-2})
I_L	Moment of inertia of the ball on its longitudinal axis (kg m^2)
I_T	Moment of inertia of the ball on its transverse axis (kg m^2)
L	Lift (N), or rolling moment (Nm)
(L_a, M_a, N_a)	(x_b, y_b, z_b) Components of the aerodynamic moment (Nm)
M	Pitching moment (Nm)
m_b	Mass of the ball, 0.42 (kg)
m_{ij}	Euler-angle transformation matrix
N	Yawing moment (Nm)
(P, Q, R)	(x_b, y_b, z_b) Components of the angular velocity vector (s^{-1})
(U, V, W)	(x_b, y_b, z_b) Components of the velocity vector (m s^{-1})

K. Seo (✉)
Faculty of Education, Art and Science, Yamagata University, Yamagata, Japan
E-mail: seo@e.yamagata-u.ac.jp
Tel.: +81-23-6284350
Fax: +81-23-6284454

O. Kobayashi
Department of Aeronautics and Astronautics, Tokai University, Hiratsuka, Japan

M. Murakami
Graduate School of Systems and Information Engineering, University of Tsukuba, Tsukuba, Japan

D. Yorita · H. Nagai · K. Asai
Department of Aerospace Engineering, Tohoku University, Sendai, Japan

$\vec{V}$	Velocity vector (m s^{-1})
V_b	Volume of the ball, 4.8 $\times$ 10^{-3} (m^3)
Y	Side force (N)
(X_a, Y_a, Z_a)	(x_b, y_b, z_b) Components of the aerodynamic force (N)
(X_E, Y_E, Z_E)	Inertial coordinate system (m)
(x_b, y_b, z_b)	Body-fixed coordinate system (m)
($\hat{x}_b, \hat{y}_b, \hat{z}_b$)	(x_b, y_b, z_b) Components of the unit vector in the body-fixed coordinate system
α	Angle of Attack (°)
Θ	Pitch angle (°)
θ_{wt}	Angle between $\vec{V}$ and $\hat{x}_b$ (°)
ρ	Air density (kg m^{-3})
Φ	Roll angle (°)
Ψ	Yaw angle (°)
$\vec{\omega}$	Angular velocity vector (revolutions per second)
(χ, ξ, η, ζ)	Quaternion parameters
$(\ )_0$	initial conditions

1 Introduction

A non-spinning punted rugby ball sometimes fluctuates during flight like a knuckle ball does in baseball. In this paper, we show that the seam of the ball produces an asymmetrical pressure distribution on the sides, and the flight trajectory fluctuates during flight. In order to investigate why this is so, we measured the aerodynamic forces acting on a non-spinning ball as functions of the angle of attack and the lace angle in a low-speed wind tunnel. Moreover, a pressure-sensitive paint (PSP) measurement was carried out on a scaled model to measure the pressure distribution on the surface. PSP consists of luminescent molecules, a polymer binder and a solvent. The mechanism of PSP measurement is based on oxygen quenching. The luminescence increases if the amount of oxygen decreases, while the amount of oxygen decreases if the pressure is low. Therefore, the lower the pressure, the brighter the luminescence. It is difficult to apply PSP to low-speed flow. The dynamic pressure at 50 m/s (1.5 kPa) is comparable to the measurement accuracy of the PSP measurement. Recently, however, there has been a breakthrough in the PSP measurement technique for low-speed flow (Yamashita et al. 2007). The key is to reduce the measurement errors. PSP measurements for a rugby ball were carried out in the same manner. Finally, the flight trajectory was simulated by numerically integrating the six degree-of-freedom non-linear equations of motion on the basis of the aerodynamic forces.

2 Force measurement

A full-size rugby ball was employed to determine the aerodynamic forces acting on it in a low-speed wind tunnel with a 1.5 m $\times$ 1.0 m rectangular nozzle. We used a commercially available ball (Triple Crown, Gilbert, the official rugby World Cup ball). The wind speed was set at 15 m/s (Holmes et al. 2006). Data were acquired with a six-component strut type balance (LMC-6524-50S, Nissho Electric Works) for 16 s using a personal computer with the aid of an A/D converter board (PCI-3120, Interface). The sampling rate was 1,000 s^{-1}. Aerodynamic force data were taken for various angles of attack, α, and lace angle, σ. There is a lace on the surface of the ball (Fig. 3b) (these days a ball generally does not have a lace on the surface; Fig. 3a). A definition of the characteristic parameters is shown in Fig. 1. Figure 1a is a side view, and Fig. 1b is a front view. The angle of attack, α, is the angle between the longitudinal axis of the ball and the wind direction. The lace angle, σ, denotes the position of the lace. With the longitudinal axis perpendicular to the wind direction ($\alpha = 90°$), the lace angle σ is defined as 0° if the lace is situated facing the wind, equals 90° when it is situated on the right and 270° when on the left. When the lace is at the back, away from the wind, σ equals 180°. Since the rolling moment and yawing moment were negligibly small (Seo et al. 2004), D, L, Y and M were measured as shown in Fig. 1. The lace angle dependence of the side force coefficient C_Y is shown in Fig. 2. It can be seen that C_Y is almost 0 at $\alpha = 0°$. There is a single periodic cycle at $\alpha = 30°$ during one rotation of the lace. However, at $\alpha = 60°$, the cycle appears fragmented and at $\alpha = 90°$ there are four cycles during one rotation. It should be noted that there are four seams on the surface. This phenomenon is confirmed by the pressure-sensitive paint (PSP) measurement in the following section.

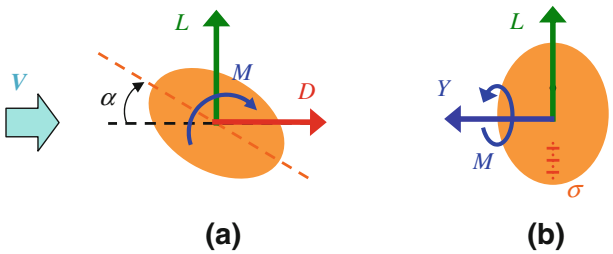

Fig. 1 Definition of aerodynamic forces and characteristic parameters. **a** *Side view* of ball. **b** *Front view* of ball

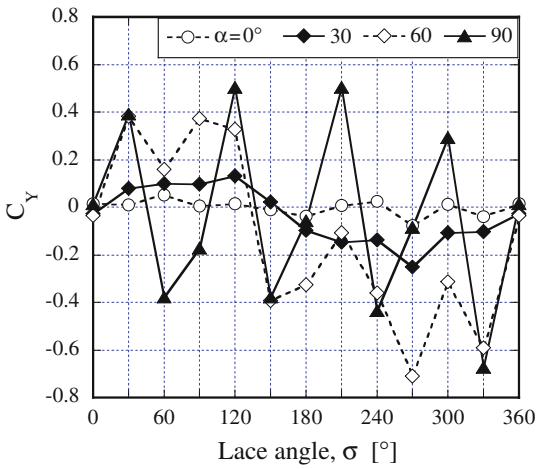

Fig. 2 The dependence of the side force coefficient, C_Y, on lace angle, σ

3 PSP measurement

A wind speed of 50 m/s was applied in this experiment. A 30% scaled model of a rugby ball was employed so that the Reynolds number would be in a practical range. The model was made of aluminum in order to prevent a temperature gradient forming in it. There were four channels on the surface representing the seams on the surface of a ball. Two semi-ellipsoids made of aluminum were joined together by screws. The shape of the semi-ellipsoid was based on caliper measurements made on a ball. The model, however, had no lace on the surface. This is because of two reasons. One reason is that these days the new type of ball does not have a lace on the surface around the valve (Fig. 3a) as mentioned above though the old type has the lace around the valve (Fig. 3b). However, both types have four seams whose depth is 1.5 mm on the surface along the longitudinal axis. The other reason is that the side force measurement revealed that there were four cycles at the angle of attack of 90° during a rotation of the lace position (Fig. 2). This result means that the four seams on the surface is more effective to change the sign of the side force than the lace. The temperature on the surface and the static pressure were also measured for calibration. A picture of the experimental set-up at $\alpha = 60°$ and $\sigma = 60°$ is shown in Fig. 4. In the front view (Fig. 4a), there is an oval shape which is clay that has been used to fill up the hole used for the screw. The electrical wires along the strut are connected to a thermocouple for temperature measurement, and the tubes are connected to a pressure transducer in a port of 0.3 mm diameter for static pressure measurement. In the PSP, the luminescent molecule is PtTFPP (Bell et al. 2001), the polymer binder is FIB (Puklin et al. 2000), and the solvent is benzene.

The results of the PSP measurement are shown in Figs. 5 and 6. These show contour maps of the pressure coefficient, C_P. Red denotes the highest value of 1.0, while blue denotes the lowest value of −2.5. The small black dots on each figure are markers to calibrate the position, and the relatively large black oval in Figs. 5d and 6 is the clay filling. The lace (seam) angle dependence at $\alpha = 90°$ is shown in Fig. 5 as well as the result on an ellipsoid (Fig. 5a), and the angle of attack dependence at $\sigma = 60°$ is shown in Fig. 6.

It can be seen from Fig. 5 that the low pressure appearing at $\sigma = 60°$ does not appear at $\sigma = 0°$ or 30° or on the ellipsoid. In other words, the seam at $\sigma = 60°$ is the trigger for initiating the low pressure, whereas

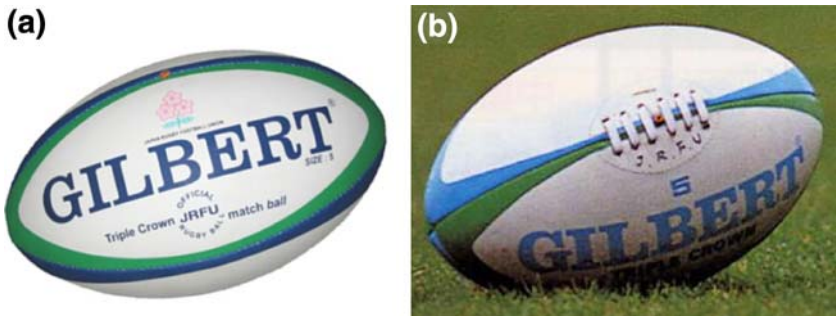

Fig. 3 The official rugby World Cup ball. **a** New type. **b** Old type

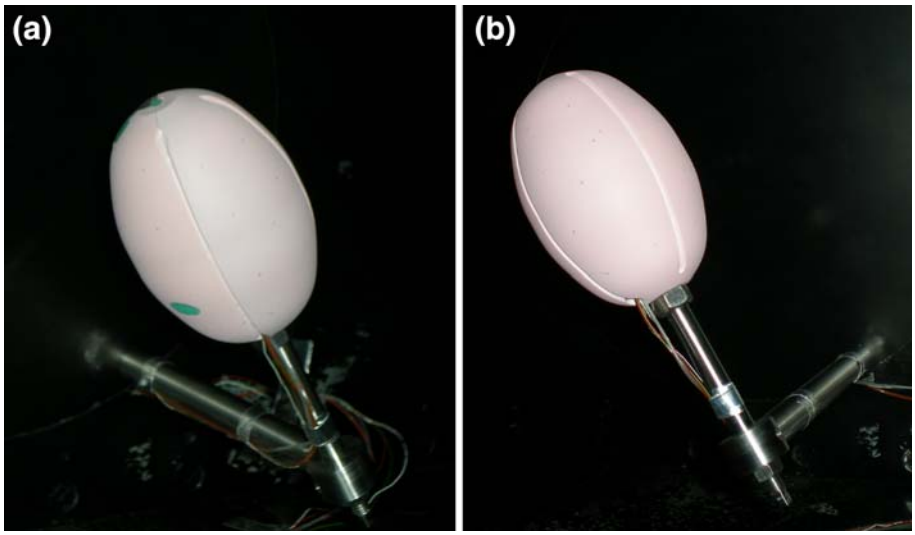

Fig. 4 The scaled model of a rugby ball. **a** *Front view* of the scaled model at $\alpha = 60°$ and $\sigma = 60°$. **b** *Back view* of the scaled model at $\alpha = 60°$ and $\sigma = 60°$

with the seam at $\sigma = 0°$ or 30°, it does not act as a trigger. It seems that the seam at $\sigma = 30°$ is too close to the stagnation point so that it does not trigger turbulence because of the low wind speed at the seam at $\sigma = 30°$. From the angle of attack dependence in Fig. 6, the low pressure appears at $\alpha = 60°$, but not at $\alpha = 0°$ or 30°. This result is consistent with Fig. 2. It can be concluded that the asymmetrical pressure distribution is due to the position of the seam. The asymmetry in the side force coefficient depends more on the position of the seam than on the position of the lace.

4 Basic equations

An inertial coordinate system is shown in Fig. 7. The origin is defined as the point of intersection of the player's own goal line and the left touch line, while the X_E-axis is along the left touch line, the Y_E-axis is from left to right along the goal line and the Z_E-axis is vertically downward. The body-fixed coordinate system for the ball is shown in Fig. 8. The origin is defined as the center of gravity of the ball. It is assumed that the geometric center of the ball coincides with the center of gravity. The x_b-axis is along the longitudinal axis of the ball, and the y_b and z_b axes are along transverse axes with the z_b-axis in the direction of the valve. Euler angles, Ψ, Θ and Φ, shown in Fig. 9, are used to describe the instantaneous attitude with respect to the inertial coordinate system. A sequence of rotations is conventionally used to describe the instantaneous attitude with respect to the inertial coordinate system. Starting with the inertial coordinate system, the following sequence is followed: (1) rotate about the Z_E-axis, nose right (positive yaw Ψ), (2)

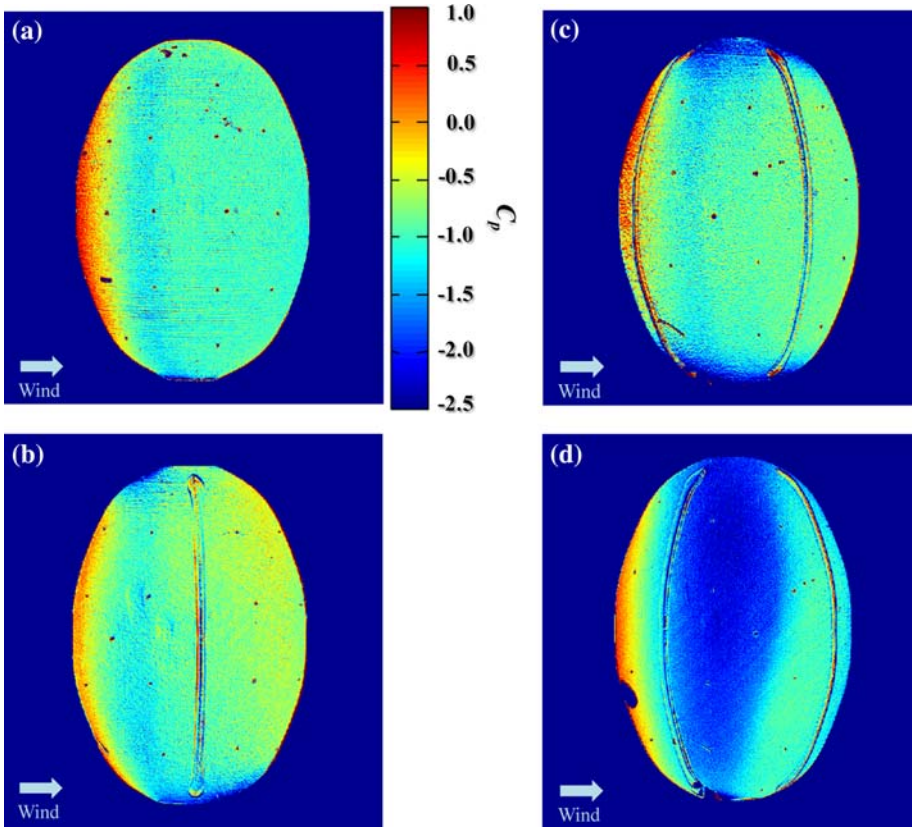

Fig. 5 Dependence of pressure distribution on lace angle at $\alpha = 90°$. **a** Pressure distribution on an ellipsoid at $\alpha = 90°$. **b** Pressure distribution at $\alpha = 90°$ and $\sigma = 0°$. **c** Pressure distribution at $\alpha = 90°$ and $\sigma = 30°$. **d** Pressure distribution at $\alpha = 90°$ and $\sigma = 60°$

rotate about the y_1 axis, nose up (positive pitch Θ), (3) rotate about the x_b-axis, right wing down (positive roll Φ).

In terms of coordinate transformations (Kato et al. 1999), we then have

$$\begin{pmatrix} \dot{X}_E \\ \dot{Y}_E \\ \dot{Z}_E \end{pmatrix} = [m_{ij}] \begin{pmatrix} U \\ V \\ W \end{pmatrix} \tag{1}$$

$$[m_{ij}] = \begin{pmatrix} \cos\Theta\cos\Psi & (\sin\Phi\sin\Theta\cos\Psi - \cos\Phi\sin\Psi) & (\cos\Phi\sin\Theta\cos\Psi + \sin\Phi\sin\Psi) \\ \cos\Theta\sin\Psi & (\sin\Phi\sin\Theta\sin\Psi + \cos\Phi\cos\Psi) & (\cos\Phi\sin\Theta\sin\Psi - \sin\Phi\cos\Psi) \\ -\sin\Theta & \sin\Phi\cos\Theta & \cos\Phi\cos\Theta \end{pmatrix}. \tag{2}$$

Here, (U, V, W) are the (x_b, y_b, z_b) components of the velocity vector as shown in Fig. 8. Since there is a mathematical singularity (Gimbal lock) at $\Theta = 90°$, quaternion parameters (χ, ξ, η, ζ) should be used instead of Euler angles (Stevens and Lewis 2003).

$$[m_{ij}] = \begin{pmatrix} (\chi^2 + \xi^2 - \eta^2 - \zeta^2) & 2(\xi\eta - \chi\zeta) & 2(\xi\zeta + \chi\eta) \\ 2(\xi\eta + \chi\zeta) & \chi^2 - \xi^2 + \eta^2 - \zeta^2 & 2(\eta\zeta - \chi\xi) \\ 2(\zeta\xi - \chi\eta) & 2(\eta\zeta + \chi\xi) & (\chi^2 + \zeta^2 - \xi^2 - \eta^2) \end{pmatrix}. \tag{3}$$

The equations of motion and moment equations are

$$\dot{U} = \frac{1}{m_b}[X_a + 2m_b g(\zeta\xi - \chi\eta)] - QW + RV \tag{4}$$

$$\dot{V} = \frac{1}{m_b}[Y_a + 2m_b g(\eta\zeta + \chi\xi)] - RU + PW \tag{5}$$

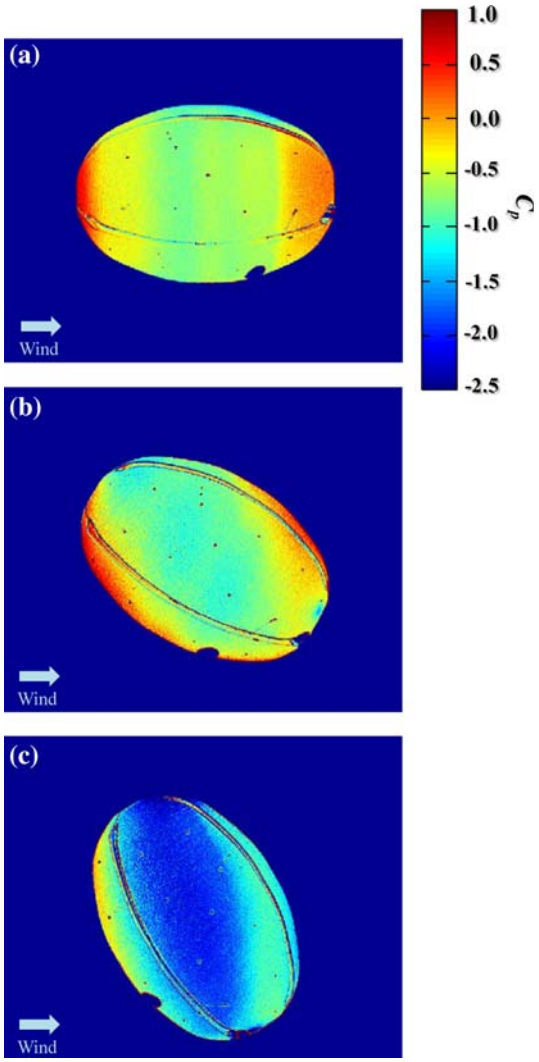

Fig. 6 Dependence of pressure distribution on the angle of attack at $\sigma = 60°$. **a** Pressure distribution at $\alpha = 0°$ and $\sigma = 60°$. **b** Pressure distribution at $\alpha = 30°$ and $\sigma = 60°$. **c** Pressure distribution at $\alpha = 60°$ and $\sigma = 60°$

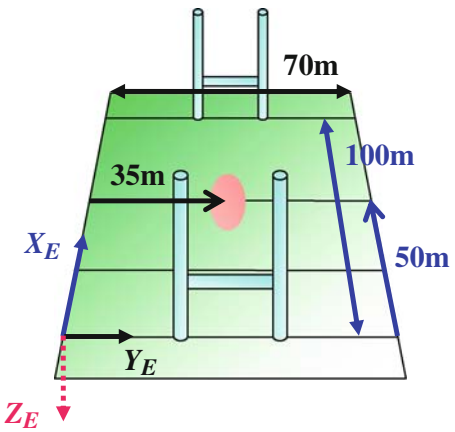

Fig. 7 Inertial coordinate system

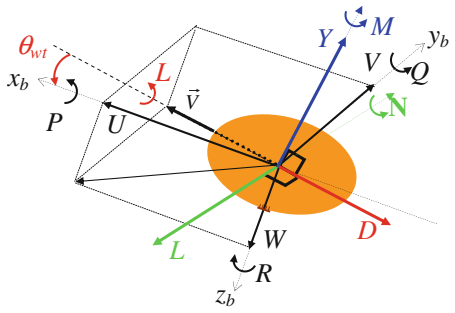

Fig. 8 Body-fixed coordinate system

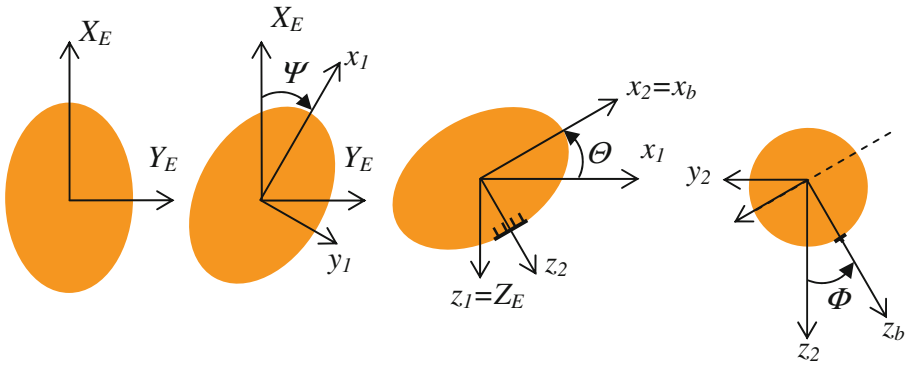

Fig. 9 Euler angles

$$\dot{W} = \frac{1}{m_b}\left[Z_a + m_b g\left(\chi^2 + \zeta^2 - \xi^2 - \eta^2\right)\right] - PV + QU \tag{6}$$

$$\dot{P} = \frac{L_a}{I_L} \tag{7}$$

$$\dot{Q} = \frac{M_a}{I_T} - PR\left(\frac{I_L}{I_T} - 1\right) \tag{8}$$

$$\dot{R} = \frac{N_a}{I_T} + PQ\left(\frac{I_L}{I_T} - 1\right). \tag{9}$$

Here, (X_a, Y_a, Z_a) are the (x_b, y_b, z_b) components of the aerodynamic force, (P, Q, R) are the (x_b, y_b, z_b) components of the angular velocity vector, m_b is the mass of the ball, g is the gravitational acceleration, (L_a, M_a, N_a) are the (x_b, y_b, z_b) components of the aerodynamic moment, and I_L and I_T are the moments of inertia of the ball on its longitudinal axis and on its transverse axis, respectively. Assuming that the rugby ball is a hollow ellipsoid, then $I_L = 0.0026$ kg m^2 and $I_T = 0.0033$ kg m^2 (Brancazio 1987).

The experimental aerodynamic data D, L and M are obtained as functions of the angle of attack from the wind tunnel experiment (Seo et al. 2006). It is necessary to convert the experimental aerodynamic data D, L, Y and M into X_a, Y_a, Z_a and L_a, M_a, N_a. The plane which contains the velocity vector $\vec{V}$ and the unit vector of the x_b component $\hat{x}_b$ is considered. Since the direction of the side force is perpendicular to this plane, the unit vector in the direction of the side force is expressed by the vector product in Eq. 10.

$$\frac{\vec{V} \times \hat{x}_b}{|\vec{V}||\hat{x}_b| \sin\theta_{\mathrm{wt}}} = \frac{W\hat{y}_b - V\hat{z}_b}{|\vec{V}|\frac{\sqrt{V^2+W^2}}{|\vec{V}|}} = \frac{W\hat{y}_b - V\hat{z}_b}{\sqrt{V^2+W^2}}. \tag{10}$$

Here, $(\hat{x}_b, \hat{y}_b, \hat{z}_b)$ are the unit vectors in the directions (x_b, y_b, z_b). The angle θ_{wt} between $\vec{V}$ and $\hat{x}_b$ is defined by Eq. 11.

$$\theta_{\mathrm{wt}} = \sin^{-1}\left(\frac{\sqrt{V^2+W^2}}{|\vec{V}|}\right). \tag{11}$$

Having derived the unit vectors in the same manner, D, L and Y can be converted into X_a, Y_a and Z_a using Eq. 12.

$$\begin{pmatrix} X_a \\ Y_a \\ Z_a \end{pmatrix} = \begin{pmatrix} -D\frac{U}{|\vec{V}|} + L\frac{\sqrt{V^2+W^2}}{|\vec{V}|} \\ -D\frac{V}{|\vec{V}|} - L\frac{UV}{\sqrt{V^2+W^2}|\vec{V}|} + Y\frac{W}{\sqrt{V^2+W^2}} \\ -D\frac{W}{|\vec{V}|} - L\frac{UW}{\sqrt{V^2+W^2}|\vec{V}|} - Y\frac{V}{\sqrt{V^2+W^2}} \end{pmatrix}. \tag{12}$$

The moments L, M and N are converted into L_a, M_a and N_a in the same manner.

$$\begin{pmatrix} L_a \\ M_a \\ N_a \end{pmatrix} = \begin{pmatrix} L\frac{U}{|\vec{V}|} - N\frac{\sqrt{V^2+W^2}}{|\vec{V}|} \\ L\frac{V}{|\vec{V}|} + M\frac{W}{\sqrt{V^2+W^2}} + N\frac{UV}{\sqrt{V^2+W^2}|\vec{V}|} \\ L\frac{W}{|\vec{V}|} - M\frac{V}{\sqrt{V^2+W^2}} + N\frac{UW}{\sqrt{V^2+W^2}|\vec{V}|} \end{pmatrix}. \tag{13}$$

Assuming $L = N = 0$, Eq. 13 can be simplified. The derivatives of the quaternion parameters (Stevens and Lewis 2003) are expressed by

$$\dot{\chi} = 0.5(-P\xi - Q\eta - R\varsigma) \tag{14}$$

$$\dot{\xi} = 0.5(P\chi - Q\varsigma + R\eta) \tag{15}$$

$$\dot{\eta} = 0.5(P\varsigma + Q\chi - R\xi) \tag{16}$$

$$\dot{\zeta} = 0.5(-P\eta + Q\xi + R\chi). \tag{17}$$

The initial quaternion parameters are expressed by

$$\chi_0 = \cos(\Phi_0/2)\cdot\cos(\Theta_0/2)\cdot\cos(\Psi_0/2) + \sin(\Phi_0/2)\cdot\sin(\Theta_0/2)\cdot\sin(\Psi_0/2) \tag{18}$$

$$\xi_0 = \sin(\Phi_0/2)\cdot\cos(\Theta_0/2)\cdot\cos(\Psi_0/2) + \cos(\Phi_0/2)\cdot\sin(\Theta_0/2)\cdot\sin(\Psi_0/2) \tag{19}$$

$$\eta_0 = \cos(\Phi_0/2)\cdot\sin(\Theta_0/2)\cdot\cos(\Psi_0/2) + \sin(\Phi_0/2)\cdot\cos(\Theta_0/2)\cdot\sin(\Psi_0/2) \tag{20}$$

$$\zeta_0 = \cos(\Phi_0/2)\cdot\cos(\Theta_0/2)\cdot\sin(\Psi_0/2) + \sin(\Phi_0/2)\cdot\sin(\Theta_0/2)\cdot\cos(\Psi_0/2). \tag{21}$$

By integrating Eqs. 1, 4 through 9, and Eq. 14 through 17 with respect to time, the flight trajectory can be obtained.

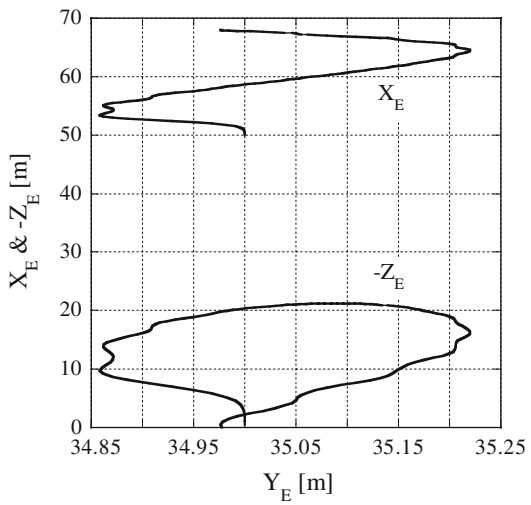

Fig. 10 Flight trajectory

5 Flight trajectory

A punted kick from the center of the field is now simulated. The initial position is assumed to be (X_E, Y_E, Z_E) = (50, 35, −0.5) as shown in Fig. 7. In order to simulate the fluctuating flight trajectory, nine initial conditions such as the magnitude and the direction of $\vec{V}_0$, the magnitude and the direction of $\vec{\omega}_0$ and the three Euler angles should be given. An example of the flight trajectory is shown in Fig. 10. In this simulation, the following initial conditions were assumed: $|\vec{V}_0| = 25\ \mathrm{m\,s^{-1}}$ with an elevation angle (flight path angle) of 70° and an azimuth angle of 0°, $|\vec{\omega}_0| = 0.5\,\mathrm{rev./s}$ with an elevation angle of 80° and an azimuth angle of 0°, $\Psi_0 = 0°$, $\Theta_0 = 70°$ and $\Phi_0 = 0°$. It can be seen that the punted kick rotating at low spin rates fluctuates from side-to-side during flight. The hang time is 4.2 s and the maximum height is 21.2 m.

6 Conclusions

The effect of the seams of a rugby ball on the side force was investigated by PSP measurement, and the flight trajectory of the punted kick was simulated. The following conclusions were obtained.

1. There are four cycles during one rotation of the lace at the angle of attack of 90°.
2. The asymmetrical pressure distribution is due to the position of the seam.
3. The punted kick rotating at low spin rates fluctuates from side-to-side during flight.

Acknowledgments This work is supported by Grant-in-Aid for Young Scientists (A).

References

Bell JH, Schairer ET, Hand LA, Mehta RD (2001) Surface pressure measurements using luminescent coatings, Annu. Rev Fluid Mech 33:155

Brancazio PJ (1987) Rigid-body dynamics of a football. Am J Phys 55:415–420

Holmes C, Jones R, Harland AR, Petzing JN (2006) Ball launch characteristics for elite rugby union players. Eng Sport 6(1):211–216

Kato K, Ohya A, Karasawa K (1999) Stability and control of airplanes, vol 11. University of Tokyo Press, Tokyo (in Japanese)

Puklin E, Carlson B, Gouin S, Costin C, Green E, Ponomerev S, Tanji H, Gouterman M (2000) Ideality of pressure-sensitive paint. I. Platinum tetra (pentafluoropheny) porphine in fluoroacrylic polymer. J Appl Poly Sci 77:2795–2804

Seo K, Kobayashi O, Murakami M (2004) Regular and irregular motion of a rugby football during flight. Eng Sport 5(1):567–573

Seo K, Kobayashi O, Murakami M (2006) Flight dynamics of the screw kick in rugby. Sports Eng 9:49–58

Stevens BL, Lewis FL (2003) Aircraft control and simulation, 2nd edn. Wiley, New York, pp 25–34

Yamashita T, Sugiura H, Nagai H, Asai K, Ishida K (2007) Pressure-sensitive paint measurement of the flow around a simplified car model. J Vis 10:289–298